nature neuroscience

Mitochondrial Ca^{2+} mobilization is a key element in olfactory signaling

Daniela Fluegge[1,5], Lisa M Moeller[1,5], Annika Cichy[1], Monika Gorin[1], Agnes Weth[2], Sophie Veitinger[1], Silvia Cainarca[3], Stefan Lohmer[3], Sabrina Corazza[3], Eva M Neuhaus[4], Werner Baumgartner[2], Jennifer Spehr[1] & Marc Spehr[1]

In olfactory sensory neurons (OSNs), cytosolic Ca^{2+} controls the gain and sensitivity of olfactory signaling. Important components of the molecular machinery that orchestrates OSN Ca^{2+} dynamics have been described, but key details are still missing. Here, we demonstrate a critical physiological role of mitochondrial Ca^{2+} mobilization in mouse OSNs. Combining a new mitochondrial Ca^{2+} imaging approach with patch-clamp recordings, organelle mobility assays and ultrastructural analyses, our study identifies mitochondria as key determinants of olfactory signaling. We show that mitochondrial Ca^{2+} mobilization during sensory stimulation shapes the cytosolic Ca^{2+} response profile in OSNs, ensures a broad dynamic response range and maintains sensitivity of the spike generation machinery. When mitochondrial function is impaired, olfactory neurons function as simple stimulus detectors rather than as intensity encoders. Moreover, we describe activity-dependent recruitment of mitochondria to olfactory knobs, a mechanism that provides a context-dependent tool for OSNs to maintain cellular homeostasis and signaling integrity.

OSNs transform the chemical energy of odor molecule–receptor binding into membrane depolarization and, ultimately, action potential discharge[1,2]. In olfactory cilia, odorant receptor[3] activation results in cyclic AMP synthesis by adenylyl cyclase[4] and opening of cyclic nucleotide–gated (CNG) ion channels[5,6]. CNG channel gating generates a depolarizing inward current carried by Na^+ and Ca^{2+}. Ciliary Ca^{2+} in turn opens a Ca^{2+}-activated Cl^- (Cl^-_{Ca}) channel[7], likely anoctamin 2 (ref. 8; see also ref. 9). Consequently, signal gain and response termination directly depend on those mechanisms that control cAMP degradation by phosphodiesterase and, more importantly[10,11], clearance of cytosolic Ca^{2+}.

In OSNs, Ca^{2+} is not only essential for gain modulation, but also critical for sensory adaptation[12]. As the dominant mechanism of olfactory adaptation, Ca^{2+}/calmodulin-dependent negative feedback modulation of the CNG channel directly shapes the stimulus–response (S–R) function of OSNs[11,13–18]. Notably, at low Ca^{2+} concentrations (<100 nM), Ca^{2+}-free calmodulin (apocalmodulin) is constitutively associated with modulatory CNG channel subunits[15]. Thus, even small changes in cytosolic Ca^{2+} concentration ($[Ca^{2+}]_c$) affect CNG channel sensitivity and, consequently, the shape of the odor response[11,19]. Therefore, $[Ca^{2+}]_c$ in OSNs must be tightly controlled[12].

Resting $[Ca^{2+}]_c$ in olfactory cilia is ~40 nM (ref. 20), but local elevations to micromolar concentrations occur during odor responses[18]. Ca^{2+} clearance from the cilia and dendritic knob has been primarily attributed to a Na^+/Ca^{2+} exchanger[21,22] (NCX), predominantly NCKX4 (ref. 23), and plasma membrane Ca^{2+}-ATPases[24,25] (PMCAs). A conceptually different approach to restoring resting $[Ca^{2+}]_c$ involves Ca^{2+} sequestration in storage organelles[26]. Although previous studies have addressed functional aspects of endoplasmic reticulum (ER)-mediated Ca^{2+} storage in OSNs[27], a physiological role of mitochondrial Ca^{2+} signaling in these cells has not been described. In general, Ca^{2+} accumulation in mitochondria serves a dual function by meeting local energy demands and shaping cytosolic Ca^{2+} signals. During $[Ca^{2+}]_c$ elevations, the negative inner mitochondrial membrane potential ($\Delta\Psi_m$) drives Ca^{2+} influx into the matrix[28] through the mitochondrial Ca^{2+} uniporter[29–31] (mCU). In neurons, Ca^{2+} clearance from the matrix is predominantly established by an organelle-specific Na^+/Ca^{2+} exchanger[32] (NCX_{mito}).

Mitochondria are highly dynamic mobile organelles that are transported at velocities between 0.3 and 1.0 μm s^{-1} (ref. 33). Local $[Ca^{2+}]_c$ elevations are instrumental in mitochondrial docking and thus provide a physiological mechanism of site-specific recruitment[34,35]. Mitochondria therefore affect neuronal Ca^{2+} signaling by acting either as mobile high-capacity sinks for bulk $[Ca^{2+}]_c$ elevations or as stationary buffers that clear Ca^{2+} in restricted microenvironments[28].

Here we investigate the function of mitochondrial Ca^{2+} dynamics in OSNs. Using mice that express a photoprotein in the mitochondrial matrix[36,37], we establish a new imaging approach that allows recording of OSN mitochondrial Ca^{2+} $[Ca^{2+}]_m$ in real time from acute slices of the main olfactory epithelium (MOE). Combining $[Ca^{2+}]_m$ and $[Ca^{2+}]_c$ imaging with patch-clamp recordings and ultrastructural analysis of OSNs, we describe activity- and Ca^{2+}-dependent recruitment of mitochondria to olfactory knobs and we provide evidence that the OSN mitochondrial network is essential in defining the input–output relationship of an odor response.

[1]Department of Chemosensation, Institute for Biology II, RWTH (Rheinisch-Westfälische Technische Hochschule) Aachen University, Aachen, Germany. [2]Department of Cellular Neurobionics, Institute for Biology II, RWTH Aachen University, Aachen, Germany. [3]Axxam SpA, Milan, Italy. [4]Charité–NeuroScience Research Center, Cluster of Excellence NeuroCure, Berlin, Germany. [5]These authors contributed equally to this work. Correspondence should be addressed to M.S. (m.spehr@sensorik.rwth-aachen.de).

Received 19 December 2011; accepted 21 February 2012; published online 25 March 2012; doi:10.1038/nn.3074

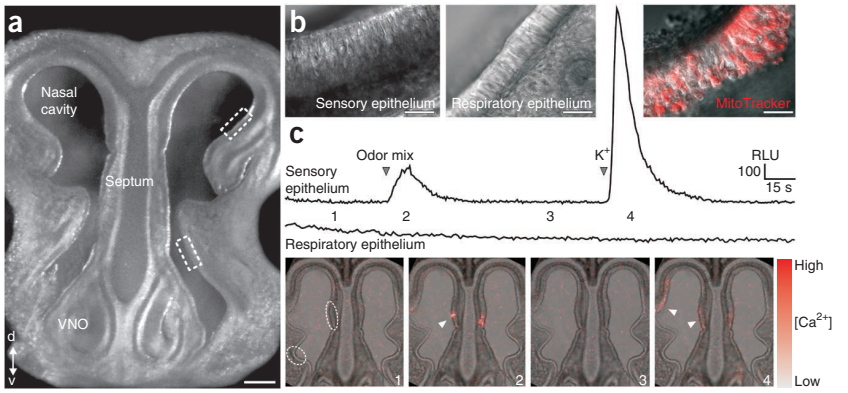

Figure 1 Bioluminescence imaging of mitochondrial Ca^{2+} dynamics in the stimulated mouse MOE. (**a**,**b**) Transmitted light image (**a**) of an acute coronal slice (250 µm thick) of the mouse rostral skull at postnatal day 2. Scale bar, 200 µm; VNO, vomeronasal organ; d, dorsal; v, ventral. White dashed boxes delimit regions of the sensory (top) and respiratory (bottom) epithelium, respectively, that are shown at a higher magnification (**b**, left and center) using infrared differential interference contrast (IR-DIC) microscopy. Also shown (**b**, right) is a merged IR-DIC and fluorescence micrograph of MOE cells labeled with MitoTracker Deep Red. Scale bars, 40 µm. (**c**) Representative original traces and corresponding single frame images from a live-cell $[Ca^{2+}]_m$ bioluminescence recording. Relative luminescence units (RLUs) from user-defined ROIs in the sensory and respiratory epithelium (frame 1, dashed circles) are plotted as a function of time. Pseudocolor bioluminescence intensity maps (gray, low $[Ca^{2+}]_m$; red, high $[Ca^{2+}]_m$) are merged with the corresponding transmitted light slice image for orientation. Single frames illustrate relative $[Ca^{2+}]_m$ at time points 1–4. Brief odor exposure (100 compounds; 10 µM; 10 s) induces a transient rise in bioluminescence that is restricted to distinct areas of the sensory epithelium (frame 2, arrowhead), whereas elevated K^+ (50 mM) triggers more broadly distributed $[Ca^{2+}]_m$ signals in the MOE (frame 4, arrowheads).

RESULTS

Mitochondrial Ca^{2+} mobilization in stimulated OSNs

So far, the role of mitochondrial Ca^{2+} signaling in OSN physiology has remained unclear. Therefore, we asked whether mitochondrial matrix Ca^{2+} increases in OSNs during odor stimulation. We developed an *in situ* method for $[Ca^{2+}]_m$ imaging in coronal slices of the mouse nose (**Fig. 1a**). Combining PhotoTopo mice[36,37], which express an enhanced matrix-targeted Ca^{2+}-sensitive photoprotein (c-Photina), and a dedicated bioluminescence microscope, we devised an imaging strategy for organelle-specific $[Ca^{2+}]_m$ monitoring (**Supplementary Fig. 1**). This approach overcomes many limitations conventionally associated with bioluminescence imaging without compromising its many advantages (irradiation- and background-free imaging, intrinsic control for cell viability, mitochondrial specificity, low buffering capacity, stable expression, and steep Ca^{2+} dependence of c-Photina).

Slice superfusion with an odor mixture (100 compounds[38], ~10 µM each; 10 s) induced transient but robust light emission in spatially confined regions of the sensory epithelium, whereas responses were never observed in the respiratory epithelium (n = 188 experiments and >90 slices; **Fig. 1b**,**c**, **Supplementary Fig. 2a** and **Supplementary Videos 1–3**). Membrane depolarization by an elevated K^+ concentration (50 mM) triggered bioluminescent signals in broader MOE areas (n = 536; **Fig. 1c**, **Supplementary Fig. 2a** and **Supplementary Videos 1–3**). At low magnification, a response delay became apparent as a function of epithelial distance from the perfusion pencil (**Supplementary Videos 1–3**). Therefore, the spread of a given response is revealed when individual frames are merged (**Supplementary Fig. 2a**). When slices were re-examined, signals proved reproducible (n = 17; **Supplementary Fig. 2b**). 'Stimulation' with control saline, however, never mediated a signal (n = 84; **Supplementary Fig. 2c**). Repeated odor stimulation during a single trial produced essentially comparable responses (n = 33; **Supplementary Fig. 2d**). With regions of interest (ROIs) derived from K^+-sensitive areas (**Supplementary Fig. 2e**,**f**), we mapped activity in response to a complex mixture versus a single odorant (**Supplementary Fig. 3**). When the MOE was arbitrarily divided into four epithelial segments (**Supplementary Fig. 3a**), stimulation with an odor cocktail did not reveal any obvious sensitivity 'hot spots' (**Supplementary Fig. 3b–d**). A defined stimulus (vanillin; 100 µM) also induced bioluminescence responses, albeit at reduced yield (n = 9; **Supplementary Fig. 3e–i**). Vanillin-responsive spots were confined to the dorsal roof (**Supplementary Fig. 3h**), the area where clusters of eGFP-labeled OSNs expressing Olfr73, the mouse olfactory receptor for eugenol (mOR-EG), are routinely found in young mOR-EG transgenic mice[39] (**Supplementary Fig. 3e**). Vanillin, a described Olfr73 agonist[39], triggered signals in regions considerably smaller than those activated by the odor mixture (**Supplementary Fig. 3i**). Thus, $[Ca^{2+}]_m$ monitoring allows coarse activity mapping in MOE slices. As the smallest responsive regions were <400 µm^2, clustered activity in relatively few cells is sufficient to produce a traceable signal. Together, the above data suggest that mitochondria in the mouse MOE accumulate Ca^{2+} upon odor exposure.

Next, we aimed to identify the cell population that exhibits odor-dependent $[Ca^{2+}]_m$ elevations. Bioluminescence could, for example, originate from any of three types of sensory neurons: those expressing canonical odorant receptors, trace amine–associated receptors (TAARs), or receptor guanylyl cyclase D (see ref. 2). When slices were stimulated in presence of adenylyl cyclase inhibitors, the odor response probability was strongly reduced, whereas the frequency of depolarization-dependent $[Ca^{2+}]_m$ signals remained unchanged (**Fig. 2**). These results indicate that neurons expressing canonical odorant receptors and/or TAARs mediate odor-specific $[Ca^{2+}]_m$ transients. Whereas signals were dependent on extracellular Ca^{2+} (**Fig. 2c**,**f**), $[Ca^{2+}]_m$ response rates remained essentially unchanged when either ER Ca^{2+} stores were irreversibly depleted by thapsigargin (**Supplementary Fig. 4a**,**d**,**e**) or Na^+/Ca^{2+} exchange was blocked by KB-R7943 or CGP37157 (**Supplementary Fig. 4b–e**,**g**). By contrast, $[Ca^{2+}]_m$ responses kinetics were changed in the presence of either drug (**Supplementary Fig. 4f**). When matrix Ca^{2+} clearance was impaired, the full duration at half maximum (FDHM) of $[Ca^{2+}]_m$ signals was significantly prolonged. These data suggest that effective Ca^{2+} extrusion from OSN mitochondria predominantly depends on NCX_{mito}.

Next, we examined whether dissipation of $\Delta\Psi_m$ disrupts mitochondrial Ca^{2+} uptake. We administered either FCCP (carbonyl cyanide 4-(trifluoromethoxy)phenylhydrazone), a reversible protonophore that selectively targets the inner mitochondrial membrane[40,41], or antimycin A, an irreversible inhibitor of respiratory chain complex III. Both drugs, applied with oligomycin to prevent ATP hydrolysis, abolished the driving force for mitochondrial Ca^{2+} uptake and, in

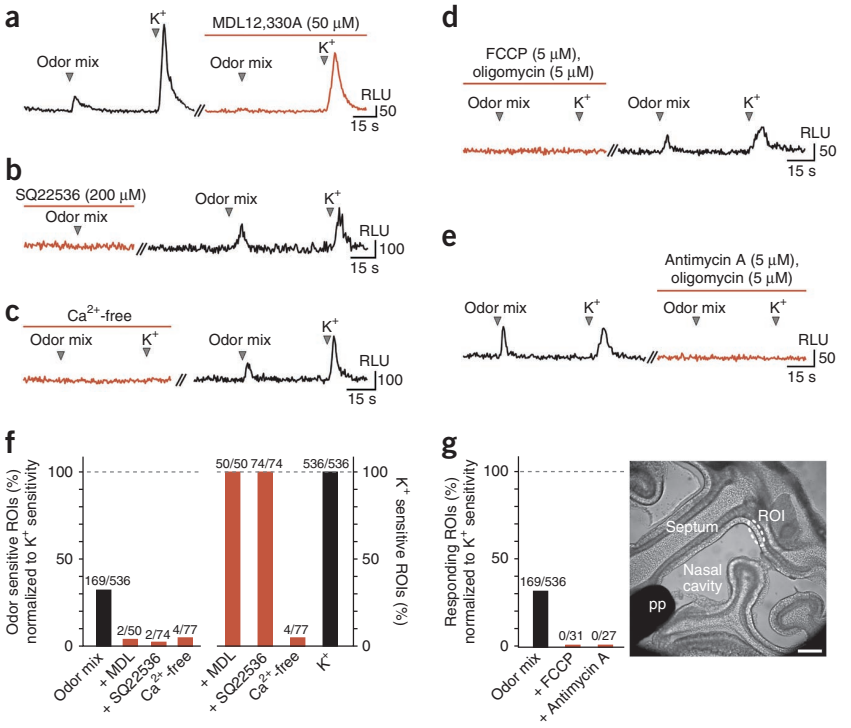

Figure 2 Mitochondria regulate Ca^{2+} shuttling during odor responses. (**a**–**c**) Representative traces (RLU versus time) illustrating odor- / K^+-dependent $[Ca^{2+}]_m$ elevations under control (black) versus adenylyl cyclase–inhibited (**a**,**b**) or Ca^{2+}-free (**c**) conditions (dark red). Red horizontal bars indicate treatment; gray arrowheads, stimulus onset. Stimulus duration, 10 s. Discontinuous traces (//) represent the same experiment. (**d**,**e**) Representative $[Ca^{2+}]_m$ traces (RLU versus time) in presence (red) and absence (black) of agents that cause $\Delta\Psi_m$ dissipation (FCCP; antimycin A; administered with oligomycin). (**f**) Bar chart depicting odor-mediated (left) and depolarization-dependent (right) $[Ca^{2+}]_m$ response probabilities relative to K^+ (50 mM) viability controls (100%; dashed horizontal lines). Whereas odor exposure triggered $[Ca^{2+}]_m$ signals in 31.5% (169/536) of trials, response probability was strongly reduced by adenylyl cyclase inhibitors (4.0% for MDL12,330A (MDL; 50 µM), $n = 50$; 2.7% for SQ22536 (200 µM); $n = 74$) and removal of external Ca^{2+} (5.2%; $n = 77$). Under the latter condition, K^+ signals were also essentially abolished (5.2%; $n = 77$). By contrast, adenylyl cyclase block did not affect K^+ signal frequency. (**g**) Bar graph illustrating odor-mediated $[Ca^{2+}]_m$ response probabilities relative to K^+ (50 mM) controls (100%). pp, perfusion pencil; scale bar, 250 µm.

MOE slices, completely disrupted $[Ca^{2+}]_m$ signals (**Fig. 2d**,**e**,**g**), confirming drug efficacy, organelle specificity of c-Photina expression and $[Ca^{2+}]_m$ dependence of the bioluminescence signals in PhotoTopo mice. Mitochondrial Ca^{2+} mobilization, however, was restored after FCCP wash-out (**Fig. 2d**). Oligomycin treatment alone had no effect (data not shown). Our results thus show that mitochondria function as effective Ca^{2+} shuttling organelles that orchestrate odor-evoked Ca^{2+} uptake and release in canonical OSNs.

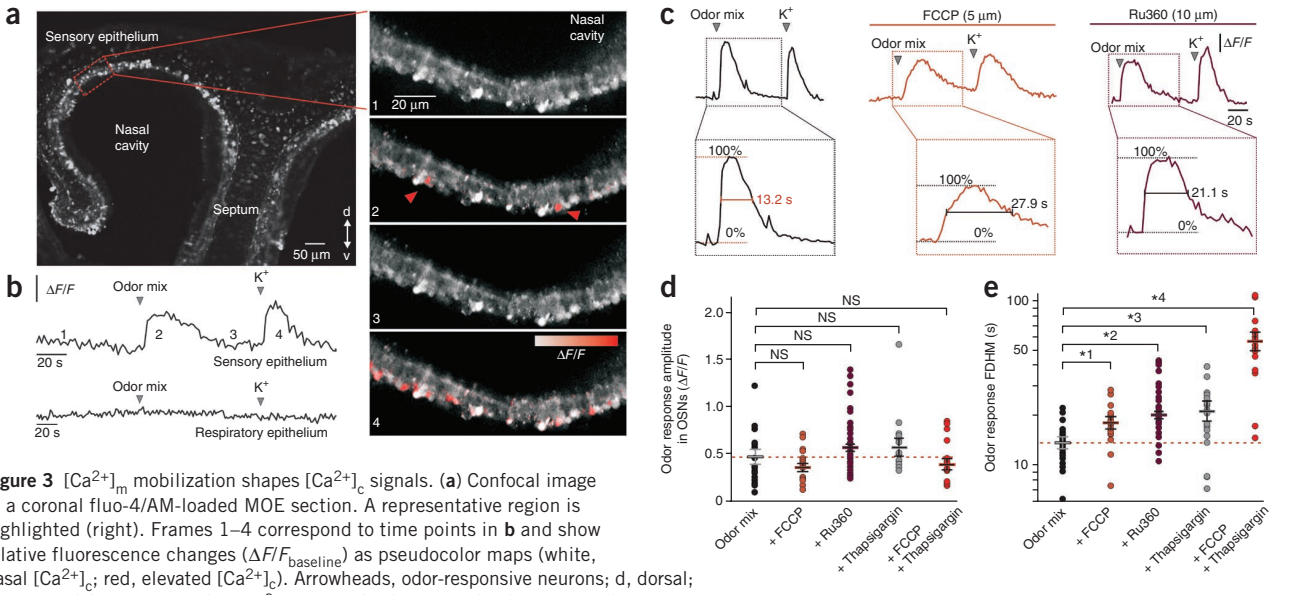

Figure 3 $[Ca^{2+}]_m$ mobilization shapes $[Ca^{2+}]_c$ signals. (**a**) Confocal image of a coronal fluo-4/AM-loaded MOE section. A representative region is highlighted (right). Frames 1–4 correspond to time points in **b** and show relative fluorescence changes ($\Delta F/F_{baseline}$) as pseudocolor maps (white, basal $[Ca^{2+}]_c$; red, elevated $[Ca^{2+}]_c$). Arrowheads, odor-responsive neurons; d, dorsal; v, ventral. (**b**) Representative $[Ca^{2+}]_c$ traces ($\Delta F/F$ versus time) from cells in the sensory (top) and respiratory epithelium (bottom) in response to odor (10 µM) and K^+ (50 mM) stimulation (10 s). (**c**) $[Ca^{2+}]_c$ traces ($\Delta F/F$ versus time) from OSNs exposed to odor and K^+ (10 s) in absence (black) or presence of FCCP (brown) or Ru360 (purple). (**d**) Odor signal intensity ($\Delta F/F$) in controls (average, dashed horizontal line) or with treatment by FCCP, Ru360, thapsigargin (10 µM) or a combination thereof. (**e**) Logarithmic FDHM plot of odor responses under control (14.26 ± 1.16 s; $n = 15$) versus treatment conditions. Impaired Ca^{2+} sequestration by mitochondria (FCCP and Ru360) or the ER (thapsigargin) prolonged signal duration (FCCP, 18.06 ± 1.31 s, $n = 15$; Ru360, 20.01 ± 0.9 s, $n = 60$; thapsigargin, 21.92 ± 2.85 s, $n = 15$). Coadministration (FCCP + thapsigargin) had a supra-additive effect (55.22 ± 6.27 s, $n = 15$). Dots represent individual experiments; bars show means ± s.e.m.; $^*P_1 = 0.01$; $^*P_2 = 0.003$, $^*P_3 = 0.01$; $^*P_4 = 0.00001$. NS, not significant.

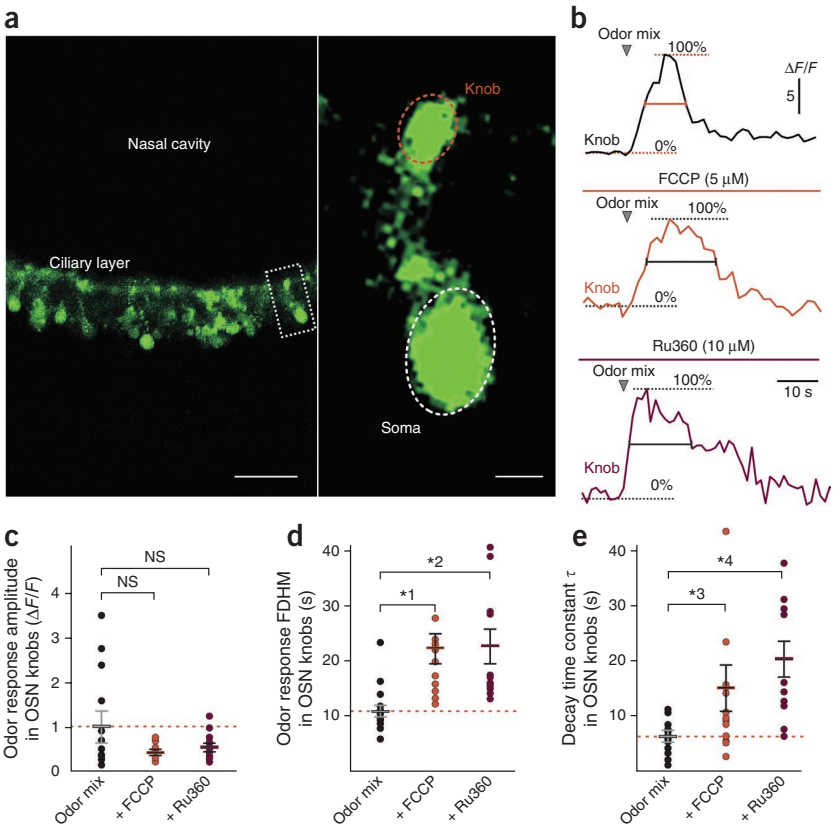

Figure 4 $[Ca^{2+}]_m$ dynamics exert local effects. (**a**) Confocal image of the fluo-4-loaded MOE (left); scale bar, 20 μm. Zooming into the boxed area shows a single OSN (right). Soma and knob are outlined as separate ROIs; scale bar, 2 μm. (**b**) Representative knob recordings ($\Delta F/F$ versus time) under control conditions (black) and during FCCP (brown) or Ru360 treatment (purple). Dotted horizontal lines mark basal and peak intensities. Solid horizontal lines show FDHM (control, 10.3 s; FCCP, 17.1 s; Ru360, 15.3 s). (**c**) Knob signals ($\Delta F/F$) in absence (1.01 ± 0.3 s; n = 15) and presence of FCCP (5 μM; 0.41 ± 0.05 s; n = 15) or Ru360 (10 μM; 0.56 ± 0.09 s; n = 11). (**d**,**e**) FDHM (**d**) and decay time constants (**e**) of odor responses in OSN knobs in absence and presence of FCCP (5 μM) or Ru360 (10 μM). Both average FDHM (control, 11.03 ± 1.2 s, n = 15; FCCP, 22.33 ± 3.0 s, n = 15; Ru360, 22.38 ± 3.1 s, n = 11) and time constant (τ) (control, 6.32 ± 0.8 s, n = 15; FCCP, 15.19 ± 3.7 s, n = 15; Ru360, 20.36 ± 3.3 s, n = 11) increased after drug treatment. In **c**–**e**, data points represent individual experiments; bars show means ± s.e.m.; $*P_1 = 0.0015$; $*P_2 = 0.0009$; $*P_3 = 0.027$; $*P_4 = 0.0001$. NS, not significant.

Mitochondria shape cytosolic Ca^{2+} signals

Upon odor stimulation, OSNs display complex $[Ca^{2+}]_c$ signals that, depending on their spatiotemporal dynamics, affect various aspects of the OSN input–output function[12,27]. Therefore, we investigated the role of mitochondria in shaping $[Ca^{2+}]_c$ responses in OSNs. By using intensity-based confocal imaging in slices (**Figs. 3** and **4** and **Supplementary Fig. 5**) and ratiometric wide-field imaging in isolated OSNs (**Supplementary Figs. 6** and **7**), we benefited from both the epithelial integrity preserved in slices and the semiquantitative high resolution data obtained by ratiometric imaging. First, we recorded $[Ca^{2+}]_c$ signals under control conditions (**Fig. 3a**,**b** and **Supplementary Video 4**). Brief odor stimulation triggered $[Ca^{2+}]_c$ transients in a subpopulation of OSNs, whereas K^+-mediated depolarization activated most neurons (**Supplementary Fig. 5a** and **Supplementary Video 5**). Cells in the respiratory epithelium never showed odor or K^+ signals (**Fig. 3b**). As expected, odor-dependent $[Ca^{2+}]_c$ responses were strongly reduced by adenylyl cyclase inhibition and essentially abolished in Ca^{2+}-free medium (**Supplementary Figs. 5b–d** and **6a**,**b**,**d**). When we disrupted mitochondrial Ca^{2+} buffering using either FCCP (**Fig. 3c** and **Supplementary Fig. 6c**), antimycin A (n = 193; data not shown) or Ru360 (an mCU inhibitor[29,30]; **Fig. 3c**), both the frequency and average amplitude of odor-dependent $[Ca^{2+}]_c$ signals remained essentially unchanged (**Fig. 3d** and **Supplementary Figs. 5d** and **6d**). Notably, both dissipation of $\Delta\Psi_m$ and mCU inhibition had pronounced effects on $[Ca^{2+}]_c$ response kinetics. We observed a significantly increased FDHM (**Fig. 3e** and **Supplementary Fig. 6e**,**f**) and decay time constant (**Supplementary Fig. 6e**,**g**). These data suggest that mitochondrial Ca^{2+} shuttling is critical for relatively fast restoration of basal $[Ca^{2+}]_c$ in OSNs. A similar function might be expected from the ER[27]. Indeed, ER depletion caused a comparably sustained $[Ca^{2+}]_c$ signal (**Fig. 3e** and **Supplementary Fig. 6e–g**). The two organelles, however, are not functionally redundant, as their simultaneous inhibition had a supra-additive effect (**Fig. 3e**).

Ca^{2+} sequestration by mitochondria or the ER affected the rising phase of odor-mediated $[Ca^{2+}]_c$ transients differently (**Supplementary Fig. 7**). The steep initial slope of the signal (10–70%) remained unchanged by inhibition of mitochondrial Ca^{2+} uptake (**Supplementary Fig. 7a**,**b**,**e**), but was significantly accelerated when ER Ca^{2+} pumps were blocked (**Supplementary Fig. 7c–e**). By contrast, $\Delta\Psi_m$ collapse decelerated the late $[Ca^{2+}]_c$ rise (70–90%). These results confirm that mitochondria and ER are both recruited for Ca^{2+} uptake during OSN stimulation. However, the two systems exhibit distinct optimal working capacities and thus shape OSN $[Ca^{2+}]_c$ dynamics during different phases of an odor response.

Mitochondria determine Ca^{2+} signals in OSN knobs

So far, we had focused on odor-evoked global $[Ca^{2+}]_c$ signals in OSNs. Next, we analyzed $[Ca^{2+}]_c$ responses in defined OSN compartments (**Fig. 4**). Notably, dissipation of $\Delta\Psi_m$ at rest induced an immediate $[Ca^{2+}]_c$ increase in the OSN soma and knob, suggesting that mitochondria also participate in the homeostatic control of basal $[Ca^{2+}]_c$ in both compartments (**Supplementary Fig. 8a**). $[Ca^{2+}]_c$ in OSN knobs remained elevated during FCCP treatment for at least 2 min (**Supplementary Fig. 8b**). When mitochondrial Ca^{2+} uptake was inhibited, odor stimulation induced $[Ca^{2+}]_c$ transients in the soma as well as the knob (**Supplementary Fig. 8c**), and average $[Ca^{2+}]_c$ signal amplitudes in OSN knobs were essentially unaffected (**Fig. 4b**,**c**). By contrast, we observed a significantly sustained response duration, an effect that was, at least in part, based on decelerated $[Ca^{2+}]_c$ clearance kinetics (**Fig. 4d**,**e**). These results show that mitochondrial Ca^{2+} dynamics affect (i) resting $[Ca^{2+}]_c$ in OSNs and (ii) local Ca^{2+} removal from the knob cytoplasm, a compartment in close proximity to the site of odor transduction.

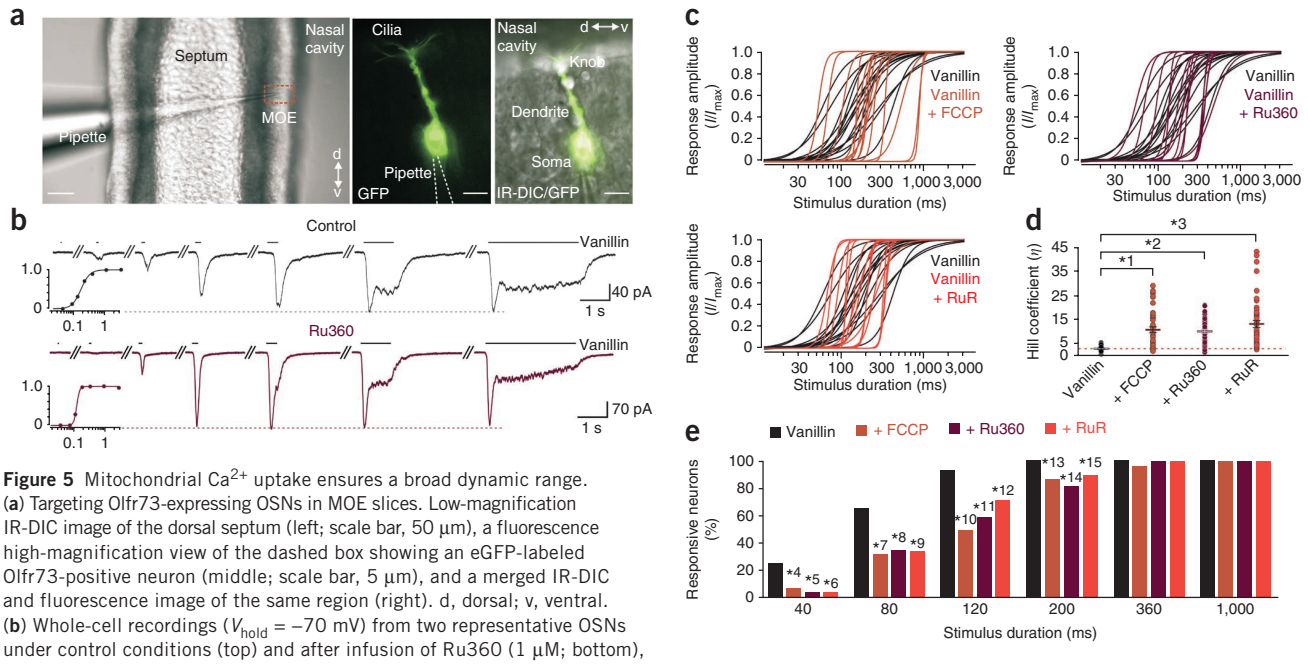

Figure 5 Mitochondrial Ca^{2+} uptake ensures a broad dynamic range. (**a**) Targeting Olfr73-expressing OSNs in MOE slices. Low-magnification IR-DIC image of the dorsal septum (left; scale bar, 50 µm), a fluorescence high-magnification view of the dashed box showing an eGFP-labeled Olfr73-positive neuron (middle; scale bar, 5 µm), and a merged IR-DIC and fluorescence image of the same region (right). d, dorsal; v, ventral. (**b**) Whole-cell recordings (V_{hold} = −70 mV) from two representative OSNs under control conditions (top) and after infusion of Ru360 (1 µM; bottom), challenged with vanillin (300 nM) at increasing duration (horizontal bars; 40 ms, 80 ms, 120 ms, 200 ms, 360 ms, 1 s, 3 s; inter-stimulus intervals, 30 s). Dashed lines indicate peak amplitudes; insets show corresponding S–R curves. (**c**) Superimposed S–R curves (I/I_{max}; Hill equation) of 15 randomly chosen OSNs under control (n = 29) and treatment conditions (FCCP, 1 µM, n = 44; Ru360, 1 µM, n = 49; RuR, 1 µM, n = 50). (**d**) Dot plot depicting individual Hill coefficients (η) of single neuron S–R curves (horizontal bars, means ± s.e.m.: control, 3.3 ± 0.2; n = 29; FCCP, 11.0 ± 1.2; Ru360, 10.4 ± 0.8; RuR, 13.4 ± 1.4). $*P_1$, $*P_2$, $*P_3$ < 0.0001. (**e**) Percentage of odor-sensitive OSNs at different pulse durations (n = 37–77). Compared to control, $*P_{15} \leq 0.05$; $*P_4$, $*P_8$, $*P_{12} \leq 0.01$; $*P_5$, $*P_6$, $*P_7$, $*P_9$, $*P_{13} \leq 0.005$; $*P_{10}$, $*P_{11}$, $*P_{14} \leq 0.001$.

Mitochondria regulate the OSN input–output function

Together with calmodulin, $[Ca^{2+}]_c$ determines the gain and sensitivity of OSN signal transduction[18]. Therefore, we next analyzed the electrophysiological properties of OSNs under control conditions and during impaired mitochondrial Ca^{2+} mobilization. We performed whole-cell patch-clamp recordings from Olfr73-expressing OSNs in acute MOE slices (**Fig. 5a**). First, we measured the S–R function for vanillin. Because detection thresholds and half-maximal effector concentrations are highly variable between OSNs expressing a defined receptor[42], we varied stimulus strength by increasing the odor pulse duration[43]. OSNs exhibited a high input resistance (3.6 ± 0.3 GΩ; n = 23) and a resting membrane potential of −76 ± 1 mV (n = 30). When vanillin (300 nM) pulses were extended from 40 ms to 3 s, current amplitudes gradually increased and saturated at pulse durations ≥1 s (**Fig. 5b** and **Supplementary Fig. 9a**). Responses were observed in 60% of all neurons. During sustained odor presentation (≥1 s), OSNs displayed a progressive response reduction, a hallmark of olfactory adaptation[44]. When we administered FCCP, Ru360 or ruthenium red (RuR; a cell-impermeable mCU inhibitor[29,31]) through the patch pipette, saturating current amplitudes were not significantly changed (**Supplementary Fig. 9b**). By contrast, when we plotted normalized receptor current amplitudes (I/I_{max}) from individual OSNs versus stimulus duration and fitted corresponding S–R curves using the Hill equation (**Fig. 5c**,**d** and **Supplementary Fig. 9a**), we observed a significantly greater average slope and thus a greatly reduced linear dynamic range when mitochondrial Ca^{2+} uptake was impaired. This increased gain slope manifests as both a shifted odor detection threshold and a rapid approach to saturation (**Fig. 5c**,**d**). Whereas we recorded small, though well defined, receptor currents in 24.5% of odor sensitive neurons on 40-ms exposure to vanillin, few OSNs responded in presence of FCCP (7.4%), Ru360 (4.1%) or RuR (4.0%) (**Fig. 5e**). At 120-ms stimulus duration, almost all (92.5%) vanillin-sensitive neurons were recruited, whereas dissipation of $\Delta\Psi_m$ or mCU inhibition significantly reduced this percentage (to 50% with FCCP, 59.2% with Ru360 and 72% with RuR). These data show that mitochondrial Ca^{2+} mobilization in OSNs is required to maintain a broad dynamic response range. When mitochondrial function is impaired, olfactory neurons function as simple stimulus detectors rather than intensity encoders.

Next, we asked whether mitochondrial Ca^{2+} buffering also affects sensory adaptation. We analyzed current decay and peak-plateau ratios during prolonged (≥3 s) stimulations (**Supplementary Fig. 9c**). The receptor current decline followed biexponential kinetics, and neither FCCP nor Ru360 or RuR changed the fast or the slow decay time constant. In addition, the average peak-plateau ratio remained essentially unaffected. During whole-cell recordings, millimolar ATP concentrations are dialyzed into the cell and the membrane potential (V_m) is set to physiological values. To test for FCCP side effects, we performed current-clamp V_m recordings over prolonged periods of time (up to 180 s) (**Supplementary Fig. 9d**,**e**). Both under control conditions and in the presence of the protonophore, V_m remained stable.

Action potential discharge ultimately represents the relevant output information that OSNs generate. Therefore, we next recorded odor-mediated firing in loose-patch configuration, a recording mode that keeps the intracellular milieu intact and does not perturb OSN input resistance. In Olfr73-expressing neurons, vanillin triggered robust time-locked spike trains at pulse durations ranging from 0.2 to 10 s (**Fig. 6** and **Supplementary Fig. 10a**,**d**,**e**). At prolonged exposure, sensory adaptation became evident as a phasic firing pattern in population peristimulus time histograms (PSTHs; 1 s bin width) (**Fig. 6a** and **Supplementary Fig. 10a**,**e**). We recorded odor-evoked mean firing rates up to 13.1 ± 1.4 Hz (2 s) under control conditions. Maximum instantaneous frequencies of individual OSNs reached 49 Hz.

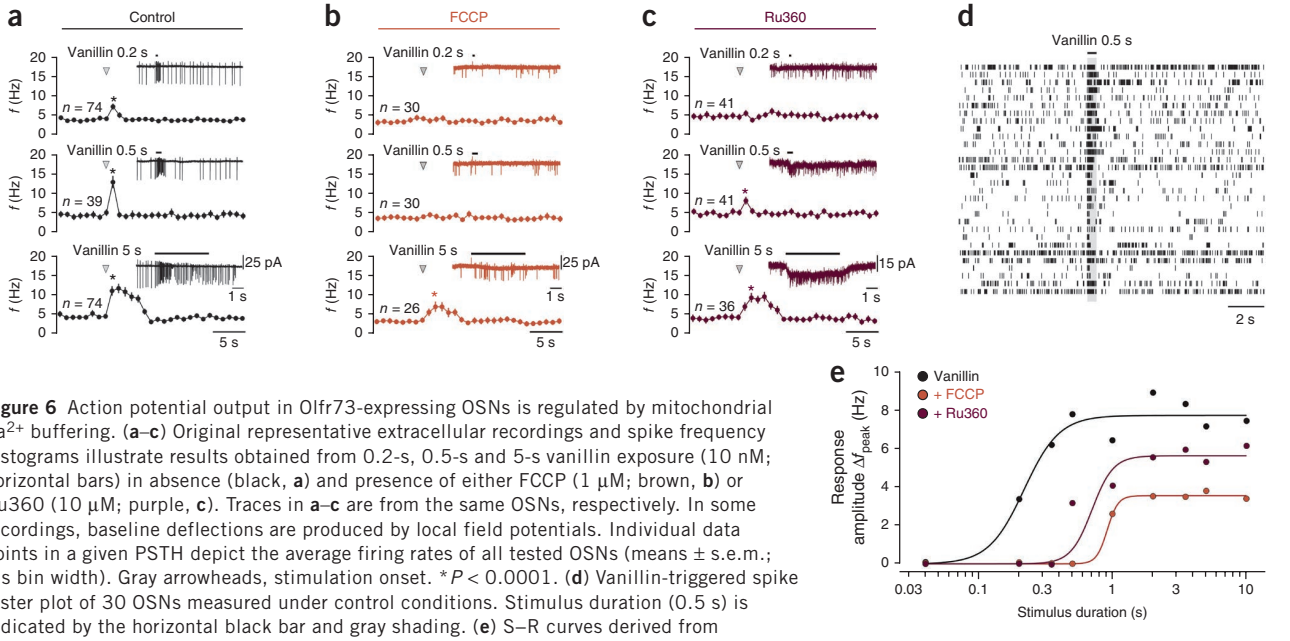

Figure 6 Action potential output in Olfr73-expressing OSNs is regulated by mitochondrial Ca^{2+} buffering. (**a**–**c**) Original representative extracellular recordings and spike frequency histograms illustrate results obtained from 0.2-s, 0.5-s and 5-s vanillin exposure (10 nM; horizontal bars) in absence (black, **a**) and presence of either FCCP (1 μM; brown, **b**) or Ru360 (10 μM; purple, **c**). Traces in **a**–**c** are from the same OSNs, respectively. In some recordings, baseline deflections are produced by local field potentials. Individual data points in a given PSTH depict the average firing rates of all tested OSNs (means ± s.e.m.; 1 s bin width). Gray arrowheads, stimulation onset. $^*P < 0.0001$. (**d**) Vanillin-triggered spike raster plot of 30 OSNs measured under control conditions. Stimulus duration (0.5 s) is indicated by the horizontal black bar and gray shading. (**e**) S–R curves derived from significant vanillin-dependent changes ($P \leq 0.01$) in average action potential discharge frequency ($\Delta f = f_{peak} - f_{baseline}$) as a function of stimulus duration and individual treatment. Curves are calculated using the Hill equation: control, $\eta = 3.3$; FCCP, $\eta = 10.9$; Ru360, $\eta = 5.5$.

Disruption of mitochondrial Ca^{2+} buffering, however, abolished any significant increase in firing rate during short (0.2–0.35 s) stimulations (**Fig. 6b**,**c**,**e** and **Supplementary Fig. 10b**,**c**). In presence of either FCCP or Ru360, a significant increase in spike frequency was only detected in response to sustained vanillin presentation (≥0.5 s with Ru360, ≥1 s with FCCP; $P < 0.0001$). Spontaneous discharge, however, remained essentially unchanged by either agent (**Supplementary Fig. 10f**). The drug-induced shift in output sensitivity and a concurrent reduction in dynamic range became apparent when spike response amplitudes ($\Delta f_{peak-baseline}$) were plotted versus pulse duration (**Fig. 6e**). Thus, mitochondrial Ca^{2+} dynamics contribute to a reliable odor-encoded output, in particular during short stimulations (that is, at low odor concentrations). Together, our data suggest that mitochondria are critical determinants of the olfactory S–R function.

Activity-dependent mitochondrial (re)distribution

Mitochondria are highly dynamic organelles[33] that might be redistributed in OSNs upon stimulation. Confocal live-cell microscopy of fluorescently labeled mitochondria in isolated OSNs of OMP-GFP mice[45] revealed preferential mitochondrial localization in perinuclear somatic

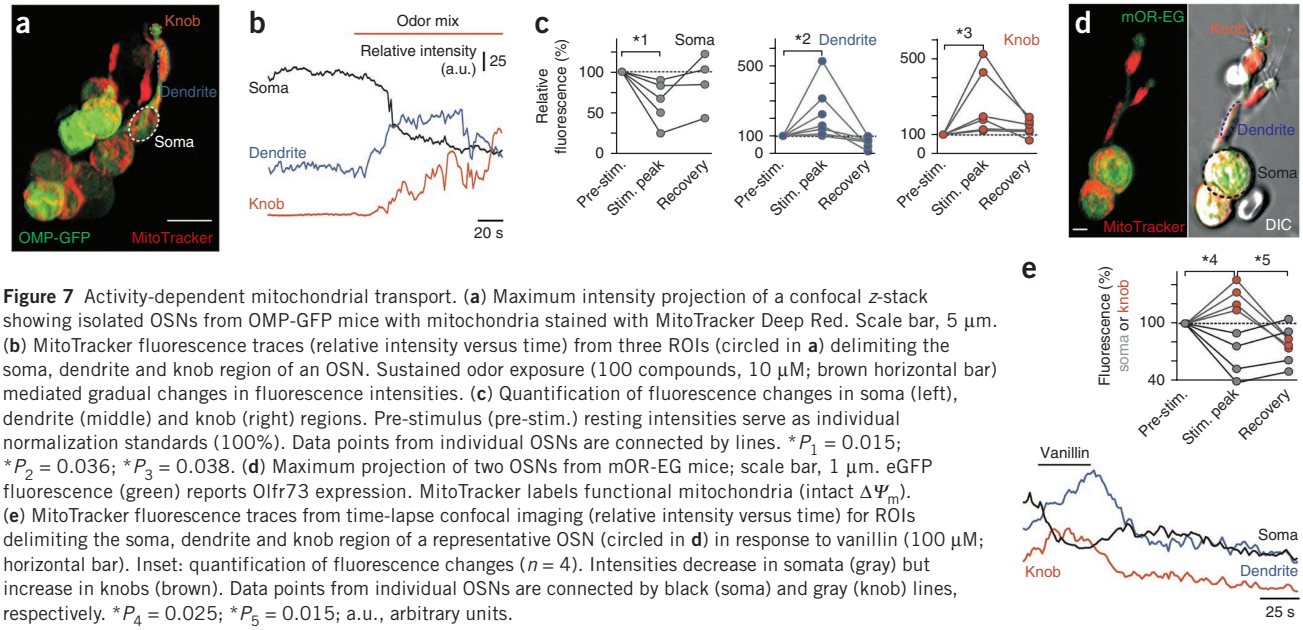

Figure 7 Activity-dependent mitochondrial transport. (**a**) Maximum intensity projection of a confocal *z*-stack showing isolated OSNs from OMP-GFP mice with mitochondria stained with MitoTracker Deep Red. Scale bar, 5 μm. (**b**) MitoTracker fluorescence traces (relative intensity versus time) from three ROIs (circled in **a**) delimiting the soma, dendrite and knob region of an OSN. Sustained odor exposure (100 compounds, 10 μM; brown horizontal bar) mediated gradual changes in fluorescence intensities. (**c**) Quantification of fluorescence changes in soma (left), dendrite (middle) and knob (right) regions. Pre-stimulus (pre-stim.) resting intensities serve as individual normalization standards (100%). Data points from individual OSNs are connected by lines. $^*P_1 = 0.015$; $^*P_2 = 0.036$; $^*P_3 = 0.038$. (**d**) Maximum projection of two OSNs from mOR-EG mice; scale bar, 1 μm. eGFP fluorescence (green) reports Olfr73 expression. MitoTracker labels functional mitochondria (intact $\Delta\Psi_m$). (**e**) MitoTracker fluorescence traces from time-lapse confocal imaging (relative intensity versus time) for ROIs delimiting the soma, dendrite and knob region of a representative OSN (circled in **d**) in response to vanillin (100 μM; horizontal bar). Inset: quantification of fluorescence changes ($n = 4$). Intensities decrease in somata (gray) but increase in knobs (brown). Data points from individual OSNs are connected by black (soma) and gray (knob) lines, respectively. $^*P_4 = 0.025$; $^*P_5 = 0.015$; a.u., arbitrary units.

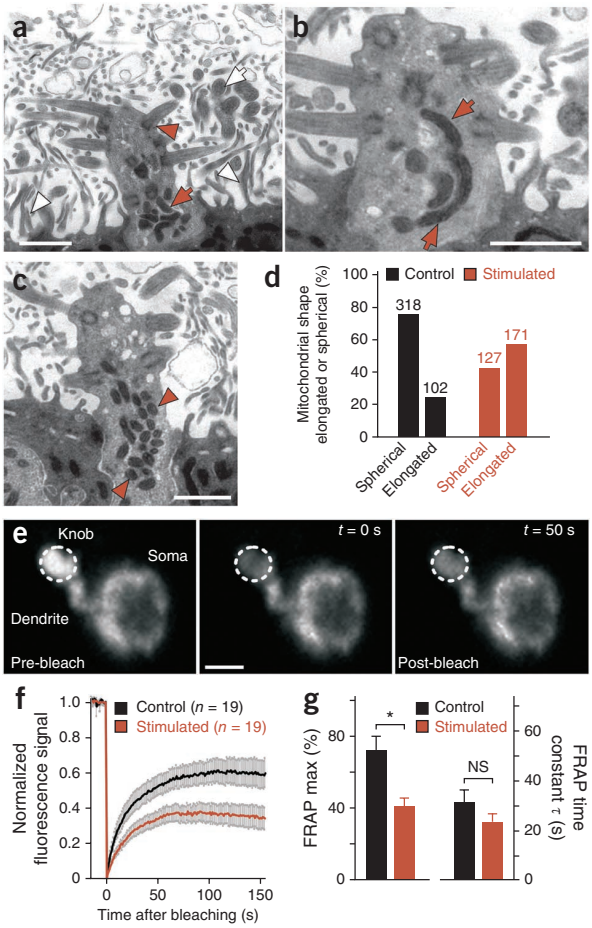

Figure 8 Recruitment of mitochondria to OSN knobs. (**a**–**c**) Representative TEM micrographs of single knobs captured from longitudinal MOE surface sections. Dendrites are surrounded by supporting cells (more electron-opaque) that extend numerous microvilli (white arrowheads, **a**) into the olfactory mucus. Scale bars, 1 µm. (**a**) Basal bodies (red arrowhead) give rise to many cilia that appear devoid of internal organelles and, when cut transversely (white arrow), display the characteristic structure of 9+2 microtubules. The knob contains various mitochondria (red arrow). (**b**,**c**) Knob mitochondria display different morphologies that we qualitatively categorized as either elongated (red arrows, **b**) or spherical (red arrowheads, **c**). (**d**) Comparison of the ratio of spherical versus elongated phenotypes in knobs from control ($n = 125$ knobs; $n = 420$ mitochondria) versus stimulated ($n = 145$ knobs; $n = 298$ mitochondria) mice. (**e**–**g**) FRAP analysis of mitochondrial mobility. (**e**) Fluorescence micrographs of an Olfr73-expressing MitoTracker-stained neuron before, during and 50 s after the knob (outlined) was photobleached; scale bar, 2 µm. (**f**) Averaged recovery curves under control conditions ($n = 19$) and during vanillin stimulation (100 µM; 60 s before and after bleaching; $n = 19$). Data (means ± s.e.m.) are normalized to pre-bleaching values and the full extent of bleaching. (**g**) Maximum (max) recovery (left) and FRAP time constants (right) under control ($n = 19$) versus stimulated ($n = 19$) conditions. Averaged τ values are determined from single exponential fits of raw traces (means ± s.e.m.). *$P = 0.002$. NS, not significant.

regions, but also robust labeling of dendritic areas (**Fig. 7a**). Using time-lapse imaging, we monitored average MitoTracker fluorescence intensities in the soma, dendrite and knob of individual OSNs. In 10 of 30 neurons, sustained exposure to a complex odor induced gradual intensity decay in the soma, whereas fluorescence increased in both the dendrite and knob (**Fig. 7b**). In responsive neurons, these shifts in fluorescence were statistically significant and reversible (**Fig. 7c**). Similar changes were never observed without stimulation ($n = 14$). We conclude that, upon intense and/or prolonged odor stimulation, mitochondria are reversibly recruited to the OSN apical dendrite and knob. In analogous experiments in isolated Olfr73-expressing neurons, we obtained qualitatively similar results upon vanillin exposure (**Fig. 7d**,**e**). Of note, no odor-dependent mitochondrial redistribution was detectable in low $[Ca^{2+}]$ bath solution ($n = 5$; data not shown), suggesting that odor-mediated Ca^{2+} influx serves as an enhancer of mitochondrial motility and/or a region-specific docking signal.

Next, we asked whether these results were also reflected at the ultrastructural level. Therefore, we analyzed mitochondrial morphology and distribution in OSN knobs from stimulated and control mice by transmission electron microscopy (TEMs; **Fig. 8a**–**c**). Although average OSN knob size did not change, we found a significant increase in mitochondrial content of knobs as a result of stimulation. Both the average area occupied by mitochondria (control, 3.05 ± 0.04%, $n = 238$; stimulated, 6.68 ± 0.05%, $n = 398$) and the average mitochondrial count per knob (control, 1.9 ± 0.3; stimulated, 2.7 ± 0.2) significantly increased ($P < 0.0001$). Moreover, when we qualitatively categorized mitochondria depending on the ratio of their longitudinal to transverse axes ($r_{l/t}$) as either spherical ($r_{l/t} \leq 2$) or elongated ($r_{l/t} > 2$), TEM analyses revealed a shift from predominantly spherical morphologies (control) to a more balanced ratio of the two phenotypes (**Fig. 8d**).

To address whether organelle accumulation in OSN dendritic endings results from mitochondrial immobilization or a more global increase in anterograde dendritic transport, we performed fluorescence recovery after photobleaching (FRAP) experiments. In isolated Olfr73-expressing neurons, we defined circular regions spanning the entire knob as photobleaching spots and monitored MitoTracker fluorescence intensities before and after bleaching (**Fig. 8e**). Normalized fluorescence recovery curves (**Fig. 8f**) followed a single exponential time course and revealed an average maximum recovery to 73% under control conditions (**Fig. 8g**). By contrast, under vanillin exposure (60 s before and after bleaching), recovery was significantly reduced (41%), whereas recovery kinetics were unaffected (**Fig. 8g**). Odor-dependent mitochondrial accumulation in OSN dendritic knobs thus results from site-specific organelle arrest of a generally highly mobile mitochondrial population.

DISCUSSION

$[Ca^{2+}]_c$ controls the gain and sensitivity of OSNs and has therefore been extensively studied[12,14,24,27]. However, an essential component of the cellular Ca^{2+} homeostasis machinery has not been investigated in olfactory signaling: mitochondria. Here, we show that mitochondrial Ca^{2+} mobilization in stimulated OSNs shapes $[Ca^{2+}]_c$ dynamics, determines the dynamic range of the S–R function, and regulates action potential discharge. Our results furthermore suggest activity-dependent and Ca^{2+}-controlled organelle recruitment to a strategic position in the olfactory knob, providing a context-dependent tool to maintain $[Ca^{2+}]_c$ signaling integrity.

So far, live-cell $[Ca^{2+}]_m$ analysis has been restricted by the lack of organelle-specific probes that (i) provide a high signal-to-noise ratio and broad dynamic range and (ii) generate enough light to measure $[Ca^{2+}]_m$ at sufficient spatiotemporal resolution[46]. Here we used a new imaging strategy to overcome these limitations. In acute MOE slices from PhotoTopo mice[36,37], we recorded $[Ca^{2+}]_m$ signals in real-time.

What is the physiological role of mitochondrial Ca^{2+} accumulation in OSNs? In general, $[Ca^{2+}]_m$ elevations provide a mechanism for meeting local energy demands[28]. As the confined geometry of OSN cilia promotes rapid collapse of ionic gradients, maintenance of ion

transport requires sustained ATP synthesis in close proximity to ciliary compartments. In addition, mitochondrial Ca^{2+} buffering likely serves a conceptually different function as a high-capacity Ca^{2+} sink that contributes to low resting Ca^{2+} and facilitates Ca^{2+} clearance during sensory stimulation. We propose that OSN mitochondria buffer a substantial amount of the odor-dependent cytosolic Ca^{2+} load. This is illustrated by a significantly decelerated cytosolic Ca^{2+} clearance when mitochondrial Ca^{2+} uptake is inhibited. Matrix Ca^{2+} accumulation might therefore be particularly important for restoring base $[Ca^{2+}]_c$ during repeated stimulation. The exact physiological function of an individual mitochondrion is contextual and dependent on the organelle's subcellular localization. In a restricted microenvironment such as the olfactory knob, inhibition of mitochondrial Ca^{2+} sequestration can have profound functional implications for local signaling mechanisms, as reported, for example, in presynaptic terminals, dendritic spines and active growth cones[33–35,47].

Our electrophysiological results revealed direct and comparable effects of $\Delta\Psi_m$ collapse and mCU inhibition on the dynamic range of OSNs. Impaired mitochondrial Ca^{2+} uptake narrowed the range and increased the slope of the S–R curve, resulting in increased sensory contrast at the expense of intensity coding. What is the mechanistic basis of mitochondrial input-output regulation? Merely insufficient energy supply can be ruled out as a cause because neurons under investigation were diffusion-loaded with ATP. It is, however, also unlikely that mitochondria located in the knob directly sequester a significant amount of those Ca^{2+} ions that enter the cell through ciliary CNG channels. Relatively small currents result in substantial intraciliary concentration changes[12], and longitudinal Ca^{2+} diffusion along the cilium is, to some extent, restricted by local buffer proteins and the close arrangement of CNG and Cl^-_{Ca} channels[48]. Yet there is no strict diffusion barrier between the olfactory knob and cilia[27]. We suggest that OSN mitochondria, in addition to NCX[21–23] and PMCA[24,25], ensure a relatively low baseline $[Ca^{2+}]_c$ of less than 100 nM (refs. 27,49). Maintaining a reduced Ca^{2+} concentration at rest is particularly important in cilia. At intraciliary $[Ca^{2+}]_c$ >100 nM, Ca^{2+} shifts CNG channel sensitivity by binding to preassociated apocalmodulin[15,18]. The sustained $[Ca^{2+}]_c$ elevation that we observed in the OSN knobs upon $\Delta\Psi_m$ dissipation would, in parallel, increase intraciliary $[Ca^{2+}]_c$. This $[Ca^{2+}]_c$ rise could thus switch CNG channels into a pseudo-adapted state and induce a right shift of the S–R curve. At the same time, elevated intraciliary $[Ca^{2+}]_c$ would bring Cl^-_{Ca} channels closer to activation threshold. Therefore, once CNG channels open, Ca^{2+} influx would rapidly amplify (and saturate) the OSN response. In concert, both mechanisms—reduced CNG channel sensitivity and concurrent facilitation of Cl^-_{Ca} channel activation—would shift the activation threshold and simultaneously increase the slope of the S–R curve, as is reflected in our experimental observations.

A critical function of mitochondrial Ca^{2+} buffering also became apparent from spike recordings. Whereas spontaneous activity and resting V_m turned out to be largely unaffected by FCCP or Ru360 exposure, the relation between stimulus intensity and action potential discharge was shifted to increased odor concentrations. This effect could, in part, directly result from changes in primary transduction (see above). However, impaired mitochondrial Ca^{2+} mobilization during action potential firing would also affect various Ca^{2+}-regulated components of the general spike generation machinery, such as Ca^{2+}-activated K^+ channels[50].

Ultrastructural findings and fluorescence-based mobility assays revealed an activity-dependent reorganization of the OSN mitochondrial network. In central neurons, mitochondria are recruited to cellular compartments with increased demand for ATP[33]. Clusters of mitochondria form in response to local $[Ca^{2+}]_c$ elevations, which function as site-specific arrest signals. We propose a similar activity-regulated immobilization pathway in OSN knobs. Our results indicate a local Ca^{2+}-dependent downregulation of mitochondrial mobility, as well as a shift in the fission/fusion balance at the docking site, thereby increasing the local mitochondrial volume by altering the overall organelle morphology. Upon stimulation, many mitochondria in OSN knobs take a more elongated shape, characteristic of immobile organelles that interact with cytoskeletal filaments and sequester Ca^{2+} more effectively[47].

In summary, our study identifies OSN mitochondria as key determinants of olfactory signaling. Mitochondrial Ca^{2+} mobilization during sensory stimulation ensures a broad S–R range and maintains sensitivity of the OSN spike generation machinery.

METHODS

Methods and any associated references are available in the online version of the paper at http://www.nature.com/natureneuroscience/.

Note: Supplementary information is available on the Nature Neuroscience website.

ACKNOWLEDGMENTS

We thank C. Engelhardt, H. Bartel and S. Lipartowski for assistance, W. Kammerloher and H.-J. Behrendt (Olympus Life Science) for placing the LV200 microscope at our disposal, and K. Touhara (University of Tokyo, Japan) and P. Mombaerts (Max Planck Institute of Biophysics, Frankfurt, Germany) for providing mouse strains. This work was funded by grants from the Volkswagen Foundation (M.S.) and the Deutsche Forschungsgemeinschaft (M.S., SP724/2-1; E.M.N., Exc257). M.S. is a Lichtenberg Professor of the Volkswagen Foundation.

AUTHOR CONTRIBUTIONS

Experiments were performed in the laboratories of M.S., W.B. and S.L. Original concept of research: D.F., S.V., S.L., E.M.N., J.S. and M.S. Research was designed by D.F., S.V., S. Cainarca, S. Corazza, E.M.N., W.B., J.S. and M.S. Data were collected by D.F., L.M.M., A.C., M.G., A.W., S.V. and J.S. and analyzed by D.F., L.M.M., J.S. and M.S. The manuscript was written by D.F., J.S. and M.S. (assistance from L.M.M., S.V., S. Corazza, W.B., E.M.N.).

COMPETING FINANCIAL INTERESTS

The authors declare competing financial interests: details accompany the full-text HTML version of the paper at http://www.nature.com/natureneuroscience/.

Published online at http://www.nature.com/natureneuroscience/.
Reprints and permissions information is available online at http://www.nature.com/reprints/index.html.

1. Firestein, S. How the olfactory system makes sense of scents. *Nature* **413**, 211–218 (2001).
2. Spehr, M. & Munger, S.D. Olfactory receptors: G protein-coupled receptors and beyond. *J. Neurochem.* **109**, 1570–1583 (2009).
3. Buck, L. & Axel, R. A novel multigene family may encode odorant receptors: a molecular basis for odor recognition. *Cell* **65**, 175–187 (1991).
4. Bakalyar, H.A. & Reed, R.R. Identification of a specialized adenylyl cyclase that may mediate odorant detection. *Science* **250**, 1403–1406 (1990).
5. Nakamura, T. & Gold, G.H. A cyclic nucleotide-gated conductance in olfactory receptor cilia. *Nature* **325**, 442–444 (1987).
6. Dhallan, R.S., Yau, K.W., Schrader, K.A. & Reed, R.R. Primary structure and functional expression of a cyclic nucleotide-activated channel from olfactory neurons. *Nature* **347**, 184–187 (1990).
7. Kleene, S.J. & Gesteland, R.C. Calcium-activated chloride conductance in frog olfactory cilia. *J. Neurosci.* **11**, 3624–3629 (1991).
8. Stephan, A.B. *et al.* ANO2 is the cilial calcium-activated chloride channel that may mediate olfactory amplification. *Proc. Natl. Acad. Sci. USA* **106**, 11776–11781 (2009).
9. Billig, G.M., Pal, B., Fidzinski, P. & Jentsch, T.J. Ca^{2+}-activated Cl^- currents are dispensable for olfaction. *Nat. Neurosci.* **14**, 763–769 (2011).
10. Cygnar, K.D. & Zhao, H. Phosphodiesterase 1C is dispensable for rapid response termination of olfactory sensory neurons. *Nat. Neurosci.* **12**, 454–462 (2009).
11. Boccaccio, A., Lagostena, L., Hagen, V. & Menini, A. Fast adaptation in mouse olfactory sensory neurons does not require the activity of phosphodiesterase. *J. Gen. Physiol.* **128**, 171–184 (2006).

12. Matthews, H.R. & Reisert, J. Calcium, the two-faced messenger of olfactory transduction and adaptation. *Curr. Opin. Neurobiol.* **13**, 469–475 (2003).
13. Reisert, J. & Matthews, H.R. Adaptation of the odour-induced response in frog olfactory receptor cells. *J. Physiol. (Lond.)* **519**, 801–813 (1999).
14. Kurahashi, T. & Menini, A. Mechanism of odorant adaptation in the olfactory receptor cell. *Nature* **385**, 725–729 (1997).
15. Bradley, J., Bonigk, W., Yau, K.W. & Frings, S. Calmodulin permanently associates with rat olfactory CNG channels under native conditions. *Nat. Neurosci.* **7**, 705–710 (2004).
16. Chen, T.Y. & Yau, K.W. Direct modulation by Ca^{2+}-calmodulin of cyclic nucleotide-activated channel of rat olfactory receptor neurons. *Nature* **368**, 545–548 (1994).
17. Munger, S.D. *et al.* Central role of the CNGA4 channel subunit in Ca^{2+}-calmodulin-dependent odor adaptation. *Science* **294**, 2172–2175 (2001).
18. Bradley, J., Reisert, J. & Frings, S. Regulation of cyclic nucleotide-gated channels. *Curr. Opin. Neurobiol.* **15**, 343–349 (2005).
19. Kleene, S.J. The electrochemical basis of odor transduction in vertebrate olfactory cilia. *Chem. Senses* **33**, 839–859 (2008).
20. Leinders-Zufall, T., Greer, C.A., Shepherd, G.M. & Zufall, F. Imaging odor-induced calcium transients in single olfactory cilia: specificity of activation and role in transduction. *J. Neurosci.* **18**, 5630–5639 (1998).
21. Noé, J., Tareilus, E., Boekhoff, I. & Breer, H. Sodium/calcium exchanger in rat olfactory neurons. *Neurochem. Int.* **30**, 523–531 (1997).
22. Reisert, J. & Matthews, H.R. Response properties of isolated mouse olfactory receptor cells. *J. Physiol. (Lond.)* **530**, 113–122 (2001).
23. Stephan, A.B. *et al.* The Na^{+}/Ca^{2+} exchanger NCKX4 governs termination and adaptation of the mammalian olfactory response. *Nat. Neurosci.* **15**, 131–137 (2011).
24. Antolin, S., Reisert, J. & Matthews, H.R. Olfactory response termination involves Ca^{2+}-ATPase in vertebrate olfactory receptor neuron cilia. *J. Gen. Physiol.* **135**, 367–378 (2010).
25. Weeraratne, S.D., Valentine, M., Cusick, M., Delay, R. & Van Houten, J.L. Plasma membrane calcium pumps in mouse olfactory sensory neurons. *Chem. Senses* **31**, 725–730 (2006).
26. Berridge, M.J., Bootman, M.D. & Roderick, H.L. Calcium signalling: dynamics, homeostasis and remodelling. *Nat. Rev. Mol. Cell Biol.* **4**, 517–529 (2003).
27. Zufall, F., Leinders-Zufall, T. & Greer, C.A. Amplification of odor-induced Ca^{2+} transients by store-operated Ca^{2+} release and its role in olfactory signal transduction. *J. Neurophysiol.* **83**, 501–512 (2000).
28. Rizzuto, R. & Pozzan, T. Microdomains of intracellular Ca^{2+}: molecular determinants and functional consequences. *Physiol. Rev.* **86**, 369–408 (2006).
29. Kirichok, Y., Krapivinsky, G. & Clapham, D.E. The mitochondrial calcium uniporter is a highly selective ion channel. *Nature* **427**, 360–364 (2004).
30. Baughman, J.M. *et al.* Integrative genomics identifies MCU as an essential component of the mitochondrial calcium uniporter. *Nature* **476**, 341–345 (2011).
31. De Stefani, D., Raffaello, A., Teardo, E., Szabo, I. & Rizzuto, R. A forty-kilodalton protein of the inner membrane is the mitochondrial calcium uniporter. *Nature* **476**, 336–340 (2011).
32. Palty, R. *et al.* NCLX is an essential component of mitochondrial Na^{+}/Ca^{2+} exchange. *Proc. Natl. Acad. Sci. USA* **107**, 436–441 (2010).
33. MacAskill, A.F. & Kittler, J.T. Control of mitochondrial transport and localization in neurons. *Trends Cell Biol.* **20**, 102–112 (2010).
34. Chang, D.T. & Reynolds, I.J. Mitochondrial trafficking and morphology in healthy and injured neurons. *Prog. Neurobiol.* **80**, 241–268 (2006).
35. Li, Z., Okamoto, K., Hayashi, Y. & Sheng, M. The importance of dendritic mitochondria in the morphogenesis and plasticity of spines and synapses. *Cell* **119**, 873–887 (2004).
36. Cainarca, S. *et al.* A photoprotein in mouse embryonic stem cells measures Ca^{2+} mobilization in cells and in animals. *PLoS ONE* **5**, e8882 (2010).
37. Veitinger, S. *et al.* Purinergic signalling mobilizes mitochondrial Ca^{2+} in mouse Sertoli cells. *J. Physiol. (Lond.)* **589**, 5033–5055 (2011).
38. Spehr, M., Wetzel, C.H., Hatt, H. & Ache, B.W. 3-Phosphoinositides modulate cyclic nucleotide signaling in olfactory receptor neurons. *Neuron* **33**, 731–739 (2002).
39. Oka, Y. *et al.* Odorant receptor map in the mouse olfactory bulb: in vivo sensitivity and specificity of receptor-defined glomeruli. *Neuron* **52**, 857–869 (2006).
40. Rizzuto, R., Simpson, A.W., Brini, M. & Pozzan, T. Rapid changes of mitochondrial Ca^{2+} revealed by specifically targeted recombinant aequorin. *Nature* **358**, 325–327 (1992).
41. Herrington, J., Park, Y.B., Babcock, D.F. & Hille, B. Dominant role of mitochondria in clearance of large Ca2+ loads from rat adrenal chromaffin cells. *Neuron* **16**, 219–228 (1996).
42. Grosmaitre, X., Vassalli, A., Mombaerts, P., Shepherd, G.M. & Ma, M. Odorant responses of olfactory sensory neurons expressing the odorant receptor MOR23: a patch clamp analysis in gene-targeted mice. *Proc. Natl. Acad. Sci. USA* **103**, 1970–1975 (2006).
43. Ben-Chaim, Y., Cheng, M.M. & Yau, K.W. Unitary response of mouse olfactory receptor neurons. *Proc. Natl. Acad. Sci. USA* **108**, 822–827 (2011).
44. Song, Y. *et al.* Olfactory CNG channel desensitization by Ca2+/CaM via the B1b subunit affects response termination but not sensitivity to recurring stimulation. *Neuron* **58**, 374–386 (2008).
45. Potter, S.M. *et al.* Structure and emergence of specific olfactory glomeruli in the mouse. *J. Neurosci.* **21**, 9713–9723 (2001).
46. Fedrizzi, L. & Brini, M. Bioluminescent Ca2+ indicators. in *Calcium Measurement Methods* (eds. Verkhratsky, A. & Petersen, O.H.) 81–100 (Humana Press, 2010).
47. Detmer, S.A. & Chan, D.C. Functions and dysfunctions of mitochondrial dynamics. *Nat. Rev. Mol. Cell Biol.* **8**, 870–879 (2007).
48. Reisert, J., Bauer, P.J., Yau, K.W. & Frings, S. The Ca-activated Cl channel and its control in rat olfactory receptor neurons. *J. Gen. Physiol.* **122**, 349–363 (2003).
49. Restrepo, D., Okada, Y. & Teeter, J.H. Odorant-regulated Ca2+ gradients in rat olfactory neurons. *J. Gen. Physiol.* **102**, 907–924 (1993).
50. Maue, R.A. & Dionne, V.E. Patch-clamp studies of isolated mouse olfactory receptor neurons. *J. Gen. Physiol.* **90**, 95–125 (1987).

ONLINE METHODS

Chemicals, solutions and stimulus presentation. The following solutions were used: (1) Extracellular solution (**S1**) containing (in mM): 145 NaCl, 5 KCl, 1 $CaCl_2$, 1 $MgCl_2$, 10 HEPES; pH 7.3 (adjusted with NaOH); 300 mOsm (adjusted with glucose). (2) Oxygenated extracellular solution (**S2**) containing (in mM): 120 NaCl, 25 $NaHCO_3$, 5 KCl, 1 $CaCl_2$, 1 $MgSO_4$, 5 BES; pH 7.3; 300 mOsm. (3) Elevated potassium solution (**S3**) containing (in mM): 100 NaCl, 50 KCl, 1 $CaCl_2$, 1 $MgCl_2$, 10 HEPES; pH 7.3 (NaOH); 300 mOsm. (4) Low Ca^{2+} extracellular solution (**S4**) containing (in mM): 135 NaCl, 5 KCl, 5 EGTA, 1.5 $CaCl_2$, 1 $MgCl_2$, 10 HEPES; pH 7.3 (NaOH); 300 mOsm. (5) Pipette solution (**S5**) containing (in mM): 143 KCl, 2 KOH, 1 EGTA, 10 HEPES, 1 Mg-ATP, 0.5 Na-GTP, 0.3 $CaCl_2$; pH 7.1 (KOH); 290 mOsm. (6) Solution for OSN isolation (**S6**) containing (in mM): 140 NaCl, 5 KCl, 5 EGTA, 4.25 $CaCl_2$, 1 $MgCl_2$, 10 HEPES, 0.09 mg/ml papain, 1 unit/ml DNase; pH 7.3 (NaOH); 300 mOsm. Free Ca^{2+} concentrations (**S1**, **S2**, **S3**: 1 mM; **S4**, **S5**: 110 nM; **S6**: 1.8 µM) were calculated using WEBMAXC STANDARD. A mixture of 100 odorants was used to increase response probability[38,51,52]. This 'cocktail' covers a range of chemical classes (for example, aldehydes, ketones, alcohols), but it is by no means a full range representation of the chemical 'odor space' the olfactory system is equipped to detect. The following inhibitors were used: MDL12,330A, SQ22536, thapsigargin, KB-R7943, CGP37157, FCCP, antimycin A, oligomycin, Ru360, ruthenium red. FCCP and antimycin A were routinely administered in conjunction with oligomycin to prevent ATP hydrolysis in the reversed mode of ATP synthase. If not stated otherwise, chemicals were purchased from Sigma (Schnelldorf, Germany). Ru360 and ruthenium red were purchased from Calbiochem (Merck, Darmstadt, Germany). Final DMSO concentrations were ≤0.1%. Cells or tissues were preincubated ≥2 min with individual agents before experiments were performed. For labeling of mitochondria, cells were incubated in **S1** (20 min; room temperature) containing cell-permeant MitoTracker Deep Red (500 nM; Molecular Probes, Karlsruhe, Germany). Stimuli and pharmacological agents were applied via an 8-in-1 multibarrel 'perfusion pencil'[37,53].

Animals and tissue preparation. All animal procedures were in compliance with the European Union legislation (Directive 86/609/EEC) and FELASA recommendations. PhotoTopo[36], C57BL/6 (Charles River Laboratories, Sulzfeld, Germany), OMP-GFP[45], and mOR-EG[39] mice were housed in groups of both sexes (room temperature; 12 h:12 h light-dark cycle; food and water available *ad libitum*). Experiments used P0–P7 pups (acute MOE slices) or young adults of either sex (a total of 87 mice). We did not observe obvious age-, strain- or gender-dependent differences. Mice were sacrificed by brief exposure to a CO_2 atmosphere and decapitation.

Acute coronal MOE tissue slices were prepared as described[54,55]. Briefly, the skin, lower jaw, teeth and palate were removed. The anterior aspect of the head was dissected, embedded in 4% low-gelling-temperature agarose, placed in ice-cold oxygenated **S2**, and coronal slices (150 µm) were cut on a VT1000S vibratome (Leica Microsystems, Nussloch, Germany). Slices were transferred to a submerged, chilled, and oxygenated (**S2**) storage chamber until use.

OSNs were isolated as described[51,52]. Briefly, the head was cut parasagittally, the septum was removed, and the MOE was carefully dissected. The tissue was incubated in **S6** (37 °C; 15 min) and transferred to **S1** for trituration using fire-polished Pasteur pipettes. Non-dissociated cells were removed (Cell Strainer nylon meshes; Becton Dickinson, Heidelberg, Germany) and single OSNs attached to concanavalin A coated dishes.

Ca^{2+} imaging using fluorescent dyes. For Ca^{2+} imaging in MOE slices, we used an upright confocal microscope DM6000CFS (Leica Microsystems) equipped with a 20×, 1.0 NA objective. Slices were incubated in fluo4/AM-containing **S1** (2 µM; 30 min; room temperature; Molecular Probes), washed, transferred to a Slice Mini Chamber (Luigs & Neumann, Ratingen, Germany), anchored (0.1 mm thick Lycra threads), and superfused with oxygenated **S2** (~3 ml/min; gravity flow). Fluo-4 was excited at 488 nm and images were acquired at 1.0 Hz (~10 µm optical thickness). Time-lapse experiments were analyzed using LAS-AF and MM-AF software (Leica Microsystems). All cells in a field of view were marked as ROIs and relative fluorescence intensities were calculated as arbitrary units.

For semiquantitative measurements, we used ratiometric wide-field imaging in isolated OSNs. Cells were loaded with fura-2/AM (2 µM; 30 min; room temperature; **S1**; Molecular Probes). Cells were washed (15 min; **S1**) and monitored using an inverted microscope (DMI4000B, Leica Microsystems) equipped for ratiometric imaging: monochromator (VisiChrome, Visitron Systems, Puchheim, Germany), 12-bit CCD camera (Coolsnap EZ, Photometrics, Tucson, AZ), and MetaFluor software (Molecular Devices, Sunnyvale, CA). Cells were viewed at 630× magnification and illuminated sequentially at 340 nm and 380 nm (5 to 0.5 Hz cycles). Ca^{2+}-dependent signals (510 nm) were calculated as the f_{340}/f_{380} intensity ratio. f_{340}/f_{380} measurements correct for unequal dye loading, bleaching, dye leakage, and differences of optical path length and cytosolic volume[56]. No cell was investigated more than once.

For illustration of $[Ca^{2+}]_c$ responses in intact slices, we generated **Supplementary Videos 4** and **5**, which show a time-lapse sequence in which averaged 'baseline' fluorescence images were subtracted from each original confocal frame, generating a high contrast ΔF sequence in which only deviations from baseline fluorescence become discernible as pseudocolor intensity changes. This ΔF sequence has then been merged with a 'static' DIC image. This way, ΔF fluorescence changes are readily appreciated and an anatomical reference is provided. However, miniature movements of the slice during an experiment result in halo artifacts in the 1–3 pixel range. These 'halos' stem from the subtraction of a 'baseline' image that is not perfectly congruent with the respective frame.

Mitochondrial Ca^{2+} imaging using a genetically encoded photoprotein. MOE slices were incubated in **S1** containing 10 µM coelenterazine (3 h; 4 °C). Next, slices were transferred to the stage of a self-contained LV200 Luminoview luminescence microscope (Olympus Europe, Hamburg, Germany) and constantly perfused (**S1**). The MOE was visualized at different magnifications (20× 0.4 NA Plan Apo objective, 60× 1.35 NA UPlanSApo objective, and 100× 1.4 NA UPlanSApo objective) and images were captured by a cooled ImageEM C9100-13 EM-CCD camera (Hamamatsu Photonics, Herrsching am Ammersee, Germany) at 1 Hz or 25 Hz frame rates. Experiments were analyzed using Cell^M Software (Olympus). Stimulus-sensitive epithelial areas were marked as individual ROIs, and relative (bio)luminescence units (RLUs) were calculated and processed as a function of time. A given MOE slice was never used for more than two experiments (usually experiments were performed on a one-trial-per-slice basis). $[Ca^{2+}]_m$ signals in response to repeated odor exposure, interleaved with negative (bath solution) and positive (K^+) controls, were reliably recorded (15 slices, 33 odor-sensitive ROIs; see **Supplementary Fig. 2d**).

Electrophysiology. MOE slices were transferred to a recording chamber (Luigs & Neumann) on an upright fixed-stage video-microscope (DM6000 FS, Leica Microsystems) equipped for infrared-optimized DIC. Slices were superfused with oxygenated **S2** (~3 ml/min; gravity flow; room temperature). Patch pipettes (5–7 MΩ) were pulled from borosilicate glass capillaries (1.50 mm OD, 0.86 mm ID; Science Products, Hofheim, Germany) on a PC-10 micropipette puller (Narishige Instruments, Tokyo, Japan), fire-polished (MF-830 Microforge; Narishige Instruments) and filled with **S5**. An agar bridge (150 mM KCl) connected reference electrode and bath solution. An EPC-10 amplifier controlled by Patchmaster 2.53 software (HEKA Elektronik, Lambrecht/Pfalz, Germany) was used for data acquisition. We monitored and compensated pipette and membrane capacitance as well as series resistance. Only neurons exhibiting stable access resistances (change <20%) were used for analysis. Signals were low-pass filtered with analog 3- and 4-pole Bessel filters (−3 dB); adjusted to one-fifth to one-third of the sampling rate (5–20 kHz, depending on protocol). Between recordings, holding potential (V_{hold}) was −70 mV. Liquid junction potentials were calculated using JPCalcW software and corrected online. Data were analyzed using FitMaster 2.20 (HEKA Elektronik) and Igor Pro 6.04 (WaveMetrics, Lake Oswego, OR) software.

To prevent dialysis of intracellular components, action potential–driven capacitive currents were recorded from OSN somata in loose-patch cell-attached configuration (pipettes filled with **S1**). Spikes were analyzed using Igor Pro functions (SpAcAn, written by Guillaume Dugué and Charly Rousseau) for detection and analysis of spontaneous events by a threshold detection algorithm. Inter-stimulus intervals were 30 s.

Transmission electron microscopy. For 60 min, C57BL/6 mice were kept under a laminar air flow hood to minimize odor exposure (control group) or mice were exposed to high concentrations of 100 different odorants (stimulated group). Animals were then sacrificed and MOE sections were subjected to ultrastructural analysis.

Tissue samples were fixed overnight in PBS (2% PFA, 2% glutaraldehyde). After washing in PBS (3x; 15 min), samples were post-fixed in 1% (w/v) OsO4 in PBS (2 h; room temperature), washed again in H_2O (3x; room temperature), and dehydrated in ascending EtOH concentrations (30%, 50%, 70%; 30 min each). Next, samples were incubated in 2% uranyl acetate (w/v) in 70% EtOH (60 min) followed by washing in 70% EtOH (30 min). Dehydration was completed by incubation in 90%, 96% and twice 100% EtOH (30 min each). Samples were then equilibrated twice in propylene oxide (SERVA Electrophoresis, Heidelberg, Germany; 30 min) followed by 50% (w/v) propylene oxide and 50% (w/v) resin (Epon 812; Serva) overnight. Next, samples were incubated twice in 100% Epon (2 h; room temperature) and embedded in Epon 812. Ultra-thin sections (90 nm) were cut (OMU3 ultra microtome (Reichert, Vienna, Austria)) and observed using a Zeiss EM10 TEM. We used morphometric analysis software (Metamorph 7.6) to calculate the mitochondrial content of knobs. All analyses were performed in a double-blind fashion.

FRAP analysis. Freshly isolated OSNs were incubated with 500 nM MitoTracker (20 min; room temperature; dye accumulation depends on an intact $\Delta\Psi_m$). Neurons were washed twice, visualized using an upright microscope (Leica DM6000 FS; water immersion objective, 63×. 0.9 NA) and superfused with **S2** (~3 ml/min; gravity flow; room temperature). Using a multi-beam confocal system with an integrated FRAP module (VT-HAWK; VisiTech Int., Sunderland, UK), images were captured at 1 Hz for at least 200 cycles using a cooled EM-CCD camera (Hamamatsu). A 642 nm laser was used for imaging (laser power <20%), a 488 nm laser for bleaching (3 s maximum output). At least 20 frames were recorded before bleaching to establish a stable baseline. Immediately after photobleaching (circular ROIs of 1.5–2.5 µm in diameter; up to 90% bleaching), fluorescence recovery was monitored and not corrected for photobleaching or background noise. The relative mobile fraction and the monoexponential recovery time constant τ were calculated for each measurement.

Data analysis. Data are reported as means ± s.e.m. from at least three independent experiments and statistical analyses were performed using paired or unpaired two-tailed *t*-tests or a chi-squared (Fisher's exact) test (**Fig. 5e**) as dictated by data distribution and experimental design. *P*-values that report statistical significance (≤0.05) are individually specified in figure legends.

In fluorescence imaging experiments, ROIs were defined to encompass single cells or cellular compartments (soma, knob) based on visually identified morphological features of dye-loaded cells at rest. In bioluminescence imaging, ROIs were defined as those epithelial regions or spots that, within a single frame, displayed contiguous activity in response to K^+ depolarization. When slices were re-examined after brief 'reloading' with coelenterazine, corresponding ROIs were defined. An increase in either bioluminescence or fluorescence intensity was judged as a stimulus-dependent response if the following two criteria were both fulfilled: (i) the peak intensity value exceeded a given threshold that was calculated as the average baseline intensity before stimulation plus an intensity value corresponding to twice the baseline intensity s.d. ($I_{resp} > I_{baseline} + 2 \times$ s.d.($I_{baseline}$))[55,57]; (ii) the increase in light intensity was observed within 10 s after stimulus application.

$[Ca^{2+}]_c$ and receptor current decay time constants (τ) were calculated by fitting individual traces to monoexponential and biexponential functions, respectively. S–R curves were fitted by the Hill equation. The FDHM was defined as the time period between the half maximum of the Ca^{2+} rise and the Ca^{2+} decay.

51. Mashukova, A., Spehr, M., Hatt, H. & Neuhaus, E.M. Beta-arrestin2-mediated internalization of mammalian odorant receptors. *J. Neurosci.* **26**, 9902–9912 (2006).
52. Michalakis, S. *et al.* Loss of CNGB1 protein leads to olfactory dysfunction and subciliary cyclic nucleotide-gated channel trapping. *J. Biol. Chem.* **281**, 35156–35166 (2006).
53. Hagendorf, S., Fluegge, D., Engelhardt, C. & Spehr, M. Homeostatic control of sensory output in basal vomeronasal neurons: activity-dependent expression of ether-a-go-go-related gene potassium channels. *J. Neurosci.* **29**, 206–221 (2009).
54. Spehr, M. *et al.* Essential role of the main olfactory system in social recognition of major histocompatibility complex peptide ligands. *J. Neurosci.* **26**, 1961–1970 (2006).
55. Ferrero, D.M. *et al.* Detection and avoidance of a carnivore odor by prey. *Proc. Natl. Acad. Sci. USA* **108**, 11235–11240 (2011).
56. Takahashi, A., Camacho, P., Lechleiter, J.D. & Herman, B. Measurement of intracellular calcium. *Physiol. Rev.* **79**, 1089–1125 (1999).
57. Rivière, S., Challet, L., Fluegge, D., Spehr, M. & Rodriguez, I. Formyl peptide receptor-like proteins are a novel family of vomeronasal chemosensors. *Nature* **459**, 574–577 (2009).

doi:10.1038/nn.3074